Multi-length scale characterization of compression on metal foam flow-field based fuel cells using X-ray computed tomography and neutron radiography

Y. Wu,[a] X. Lu,[a] J. I. S. Cho,[a,b] L. Rasha,[a] M. Whiteley,[a,c] T. P. Neville,[a] R. Ziesche, [a] N. Kardjilov,[d] H. Markötter, [d] I. Manke,[d] X. Zhang,[e] P. R. Shearing,[a,c] D. J. L. Brett[a,c]*

[a]*Electrochemical Innovation Lab (EIL), Department of Chemical Engineering, University College London, London WC1E 7JE, United Kingdom.*
[b]*EPSRC "Frontier Engineering" Centre for Nature Inspired Engineering & Department of Chemical Engineering, University College London, London WC1E 7JE,United Kingdom.*
[c]*Advanced Propulsion Lab (APL), University College London, London WC1E 7JE, United Kingdom*
[d]*Helmholtz-Zentrum Berlin (HZB), Hahn-Meitner-Platz 1, 14109 Berlin, Germany*
[e]*School of Electrical Engineering, Southwest Jiaotong University, Chengdu, Sichuan Province 610031, China*

Email: d.brett@ucl.ac.uk (D. J. L. Brett)

Abstract

The mechanical compression of metal foam flow-field based polymer electrolyte fuel cells (PEFCs) is critical in determining the interfacial contact resistance with gas diffusion layers (GDLs), reactant flow and water management. The distinct scale between the pore structure of metal foams and the entire flow-field warrant a multi-length scale characterization that combines ex-situ tests of compressed metal foam samples and in-operando analysis of operating PEFCs using X-ray computed tomography (CT) and neutron radiography. An optimal 'medium' compression was found to deliver a peak power density of 853 mW cm^{-2}. The X-ray CT data indicates that the compression process significantly decreases the mean pore size and narrows the pore size distribution of metal foams. Simulation results suggest compressing metal foam increases the pressure drop and gas velocity, improving the convective liquid water removal. This is in agreement with the neutron imaging results that demonstrates an increase in the mass of accumulated liquid water with minimum compression compared to the medium and maximum compression cases. The results show that a balance between Ohmic resistance, water removal capacity and parasitic power is imperative for the optimal performance of metal foam based PEFCs.

Keywords: Fuel cell; Compression effect; Metal foam microstructure; Neutron radiography; X-ray CT

1. Introduction

Flow-fields are essential components for various types of energy systems, such as fuel cells, water electrolysers and combustors, etc. [1]-[5] In the case of polymer electrolyte fuel cells (PEFCs), flow-fields are responsible for reactant distribution and product removal across the active area which dictate the performance, efficiency and longevity of PEFCs [6][8]. Parallel and serpentine are amongst the first channel designs developed and remain the industrial standard due to their manufacturing simplicity and respectable performance they generate [9]-[13]. The pursuit for next generation flow-field design continues, however, not only circumvent issues pertaining to fuel cell performance and longevity but to improve overall system efficiency and manufacturability. [14]-[16].

Amongst numerous flow-field designs proposed thus far [17]-[22], metal foam is a promising candidate to address this problem [23]. This design could improve the flow distribution uniformity across the active area due to their favourable pore connectivity and numerous gas pathways [24]. Numerous researchers have examined the influence of flow-field separators, water management, and coating methods on the performance of metal foam based PEFCs [25]-[34]. In addition, studies report that PEFCs performance is strongly affected by the compression ratios of the metal foam [35]-[38]. A previous study showed substantially lower performance of a PEFC using uncompressed foam as flow-field than that of serpentine. However, the PEFC performance was significantly improved when the foam was compressed from 1000 μm to 150 μm [35]. Recently, a study was conducted that combines a compression testing system with X-ray computed tomography (CT) to investigate the mechanical behaviour of metal foam flow-field inside a PEFC. A 42% improvement in maximum power density was observed upon increase in foam compression ratio from 20% to 70% [36]. The authors attribute the performance improvement to the lower interfacial contact resistance between the foam and the GDL. However, the compression effect on microstructural properties and the consequent gas transport parameters across metal foam is not well understood.

An in-depth understanding of microstructural properties and gas transport parameters of compressed metal foams is indispensable for optimizing their design rules. Microstructural properties of the porous media, such as porosity, pore size distribution (PSD), tortuosity and permeability are often used to estimate the gas diffusion resistance [39],[40]. These properties can be acquired from image analysis

[41], [42] and modelling of mass/heat flux on the reconstructed 3D microstructure of the porous sample acquired using X-ray CT [43]-[47]. X-ray CT has been widely employed in PEFC research, including characterizing the effect of compression [48] [49] and hot pressing [50] on the morphological structure of GDLs.

In terms of water management, we expect contrasting water removal characteristics across metal foam at different compression ratios due to change in pressure drop. Since water management is a key element dictating PEFC performance and durability [51]-[53], it is important to characterize the effect of compression on the water management of metal foam flow-field based PEFCs.

The ability of neutron to penetrate through metal has led to a huge breakthrough in fuel cell research, particularly in the field of water visualization [54] [55]. This method has been applied to characterize the effect of flow-field designs, compression pressures and operating conditions [56]-[61] on PEFC water management. Recently, neutron radiography has been employed to compare the water management of metal foam and serpentine flow-field based PEFCs [62]. More uniform water distribution was observed for metal foam case due to the absence of a land/channel configuration. However, the metal foam flow-field suffered excess flooding at low current densities from substantially lower gas flow velocity. The work also suggested that altering foam microstructure could partly mitigate flooding in metal foam flow-field based PEFCs.

This study aims to shed light on the effect of compression on various microstructural properties, gas transport parameters and water management characteristics of metal foam flow-field based PEFCs. The difference in length scale of metal pore and the metal foam as a whole requires a sensible trade-off between image field-of-view and resolution. A multi-length scale characterization is therefore required. Here, an approach is used which combines *ex-situ* characterization of compressed metal foam samples with X-ray CT and *in-operando* analysis of operating PEFCs using neutron radiography. Pore structure extracted from X-ray CT images is employed to simulate the gas transport in metal foams under different compression ratios. Additionally, a series of measurements are performed to record the corresponding voltages and Ohmic resistances of metal foam flow-field based PEFCs. Therefore, this study fills a gap in the literature and for the first time combined experimental (X-ray CT for 3D structure,

while neutron imaging for water distribution) with flow modelling to examine the effect of mechanical compression on metal foam flow-field based PEFCs.

2. Experimental setup

This section details the experimental setup used in the present work, including the fuel cell design and testing, metal foam sample preparation, X-ray CT scanning, gas flow simulation and neutron radiography.

2.1. Fuel cell design and testing

A 25 cm^2 membrane electrode assembly (MEA) was assembled using commercial gas diffusion electrodes (GDEs). The specifications and manufacturing steps of the MEA used in this study is outlined elsewhere. [57] [60].

A single-channel serpentine flow-field was used on the anode. A 1.6 mm thick uncompressed graphene-coated nickel foam (Six Carbon Technology, China) was placed in the cathode between the MEA and manifold. Compression ratio control was achieved through the appropriate selection of gasket thickness (1.5, 1.0 and 0.5 mm). The same torque (1.4 Nm) [57] was applied to tie-bolts at the end-plate to compress the PEFC. The corresponding compression ratio values are 6 %, 37 % and 69 %, respectively. The selected compression ratios agree well with previously published works (up to 85%) [35], [36]. The stoichiometric ratio of dry air and hydrogen (99.995%) was kept constant at 3 and 1.5, respectively, using digital mass flow controllers (Bronkhorst, UK). We used Scribner 840 to record fuel cell Ohmic resistance via the high frequency resistance (HFR). The fuel cell temperature was maintained at 40 ˚C throughout the experiment. A diagram of the PEFC set-up and test rig are found in [62].

2.2 X-ray computed tomography (X-ray CT)

Three 2.0 mm diameter pristine metal foam discs (1.6 mm thick) were pre-compressed to 1.5, 1 and 0.5 mm thick, corresponding to the compression ratios of 6%, 37% and 69%, respectively. The microstructure of the compressed metal foam samples was obtained using a laboratory X-ray CT system, ZEISS Xradia 520 Versa (Carl Zeiss, USA). The Versa operates with tungsten anode producing

characteristic X-ray emission peaks at 59.3 keV. This instrument operates with cone-beam and source voltage of 40 kV. Detailed scanning parameters are shown in Table 1. Zeiss XM Reconstructor software was used to reconstruct these images into a 3D volume. The reconstructed sample volumes were segmented into solid and pore phase using Avizo V9.0 (ThermoFisher Scientific, USA), as seen in Fig. 1 (g, h). The same software was employed to measure the pore size distribution, porosity and tortuosity of metal foams under different compression ratios.

Table 1 Imaging parameters for the metal foam and fuel cell

	Pixel size (μm)	Field of view (mm^2)	Exposure time (s)
Metal foam sample (X-ray CT)	1.08	2.19×2.19	5
Fuel cell (Neutron radiography)	26	56×67	5

2.3 Gas flow simulation

The reconstructed 3D volume of the compressed metal foam samples was imported to the CFD software Star-CCM+ (Siemens industry software inc., USA) for the simulation [43]. Here, Darcy's law is applied to extract the permeability of the metal foam under different compression ratios [63],

$$\frac{\partial P}{\partial x} = -\frac{\mu}{k} v \tag{1}$$

where μ and v are the dynamic viscosity (kg m^{-1} s^{-1}) and volume-averaged velocity (m s^{-1}) of air, respectively, k is the permeability (m^2) of the compressed metal foam, P is the pressure (Pa) and x is the distance (m) in the flow direction. The gas inlet flow rate was set so stoichiometric ratio of 3. A no-slip condition was assigned at the metal foam surface. Simulation parameters are detailed in Table 2.

Table 2 Parameters and conditions of the gas flow simulations for the metal foam sample.

Mesh type	Polyhedral volume mesh
Number of cells	1.8 million
Inlet (air)	$2.82e^{-5}$ g s^{-1}
Outlet	1 atm
Reaction source	1.5 A cm^{-2}
Sample dimension	1.26 × 1.26 × (0.5/1/1.5) mm^3

2.4 Neutron radiography

Neutron imaging of operating PEFCs was performed at the CONRAD neutron beamline facility in Helmholtz-Zentrum Berlin (HZB) [64]. The beam is formed by a neutron guide and an additional collimation system, and is transmitted through the PEFC. The detector consisted of a CCD digital camera (Andor DW436N-BV) facing a LiF/ZnS neutron scintillator screen. The neutron scintillator converts neutron flux into light emission, which is then detected by the CCD camera [57]. A through plane orientation was used to visualize water distribution across the entire active area of the PEFCs. Images taken during cell operation were normalised to a dry image taken at the beginning of each experiment to isolate liquid water. This process is shown Fig. 1 (b-d). The Beer-Lambert law was used to calculate water thickness [60].

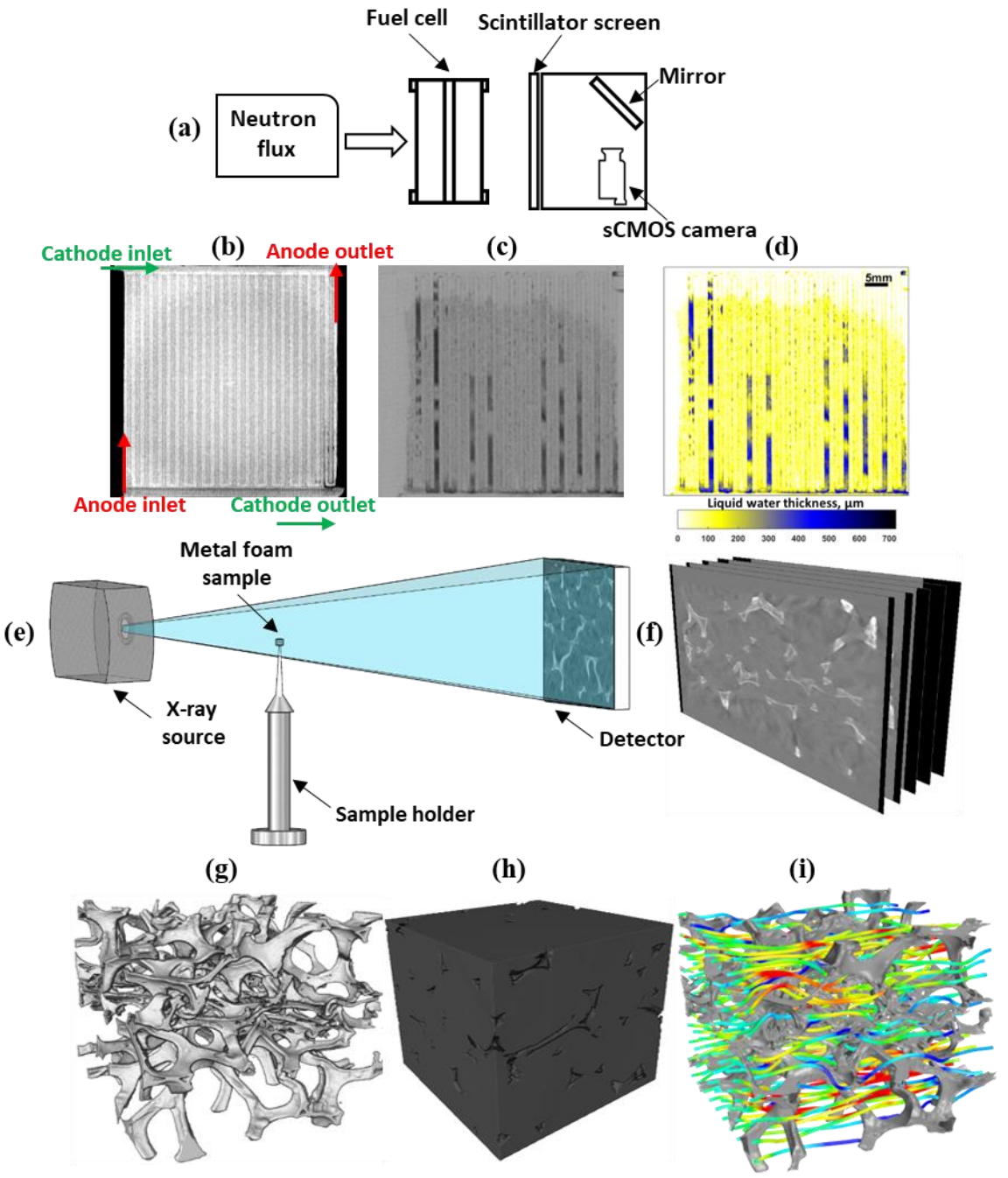

Fig. 1 Illustration of the workflow in this study: (a) schematic of neutron radiography set-up. Neutron radiograph of the (b) dry and (c) 'working' PEFC (taken during operation at 500 mA cm^{-2}); (d) averaged liquid water thickness distribution during galvanostatic operation at 500 mA cm^{-2}; (e) schematic of the X-ray micro-CT set-up; (f) reconstructed slices of the metal foam sample; 3D volume rendering of the segmented (g) solid phase (metal foam) and (h) pore space; (i) gas flow simulation through the metal foam to extract the effective transport parameters.

3. Results and discussion

Current sweep experiments were carried out by incrementally changing current density every 1200 s at 200 mA cm^{-2} intervals from open circuit voltage (OCV). Each polarization was repeated twice and

averaged. Fig. 2 (a) compares the cell performance under three different compression ratios (6 %, 37 % and 69 %). The PEFC with medium compression (37 %) yielded the best performance with ~2 % and ~8 % improvement in performance at 200 mA cm^{-2} with respect to high and low compression cases. A greater improvement in performance is observed at high current densities, where the voltage of the PEFC with medium compression is approximately 9 % and 50 % higher than that of the maximum and minimum compression at 1600 mA cm^{-2}. In terms of power density, a peak power density of 853 mW cm^{-2} was recorded for medium compression, followed by maximum (780 mW cm^{-2}) and minimum compression (568 mW cm^{-2}). The lowest performance of the PEFC with minimum compression can be insufficient GDL/ metal foam contact that led to high contact resistance. Although increasing the compression ratio alleviates these issues [35]-[38], excess compression should be avoided as it decreases the pore size of metal foams, leading to mass transfer limitations and performance loss. This is in agreement with a previous study where moderate compression can enhance the performance of metal foam flow-field based PEFCs [37]. Besides, this performance agrees with those found in previous metal foam studies (500-1000 mW cm^{-2}) [35]-[38].

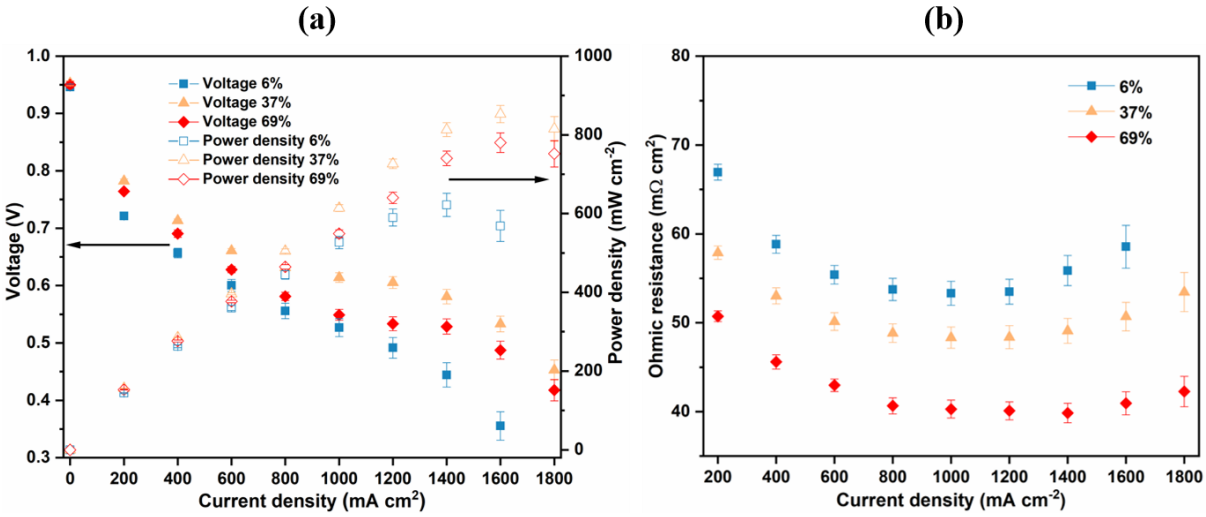

Fig. 2 Effect of compression ratio (6 %, 37 % and 69 %) on (a) polarization performance and (b) Ohmic resistance of metal foam flow-field based PEFCs measured by electrochemical impedance spectroscopy.

The Ohmic resistance of a PEFC can be estimated from high-frequency resistance (HFR) using electrochemical impedance spectroscopy. Since mechanical compression and cell temperature were kept constant throughout the experiment, any change in HFR during experiment was assumed a direct

consequence of the change in membrane hydration [65]. The change in HFR with respect to current density for metal foam PEFCs under different compression ratios is presented in Fig. 2 (b). In general, the higher compression ratio leads to a decrease in Ohmic resistance. The lowest HFR value recorded for the maximum compression case is approximately 10 % and 34 % lower than that of the medium and minimum compression, respectively. We attribute this to improved GDL/metal foam contact [36]. One feature shared amongst the three compression ratios is improved membrane hydration with current density due to elevated liquid water generation. The HFR starts to rise above 1000-1400 mA cm^{-2} as higher internal fuel cell temperature dehydrates the membrane [66].

To identify the root cause of the performance difference amongst three compression ratios, the microstructural properties and gas transport parameters of pre-compressed metal foam samples were characterized and analysed using X-ray CT. The side and top view of the compressed metal foams after segmenting the void and foam zones from the entire reconstructed volume are shown in Fig. 3. The structure of the metal foam is similar viewed from the top in Fig. 3 (d-f), implying a trivial effect of compression on the through-plane pore morphology (size) and thus the mass transport property. In contrast, the deformations of the foam structure are clearly visible at the different compression levels from the side as shown in Fig. 3 (a-c). Although smaller in-plane pores of metal foams can induce higher pressure drop [37], the smaller pores would hamper the gas transport if the foams are overly compressed. It is therefore important to optimize the compression level of metal foams. One should be noticed that other components of PEFCs may also be influenced by the assembly process. For example, X-ray CT images [36] show significant penetration of foam into the GDL when the foam flow-fields are compressed with a MEA, whereas the membrane shows no notable change.

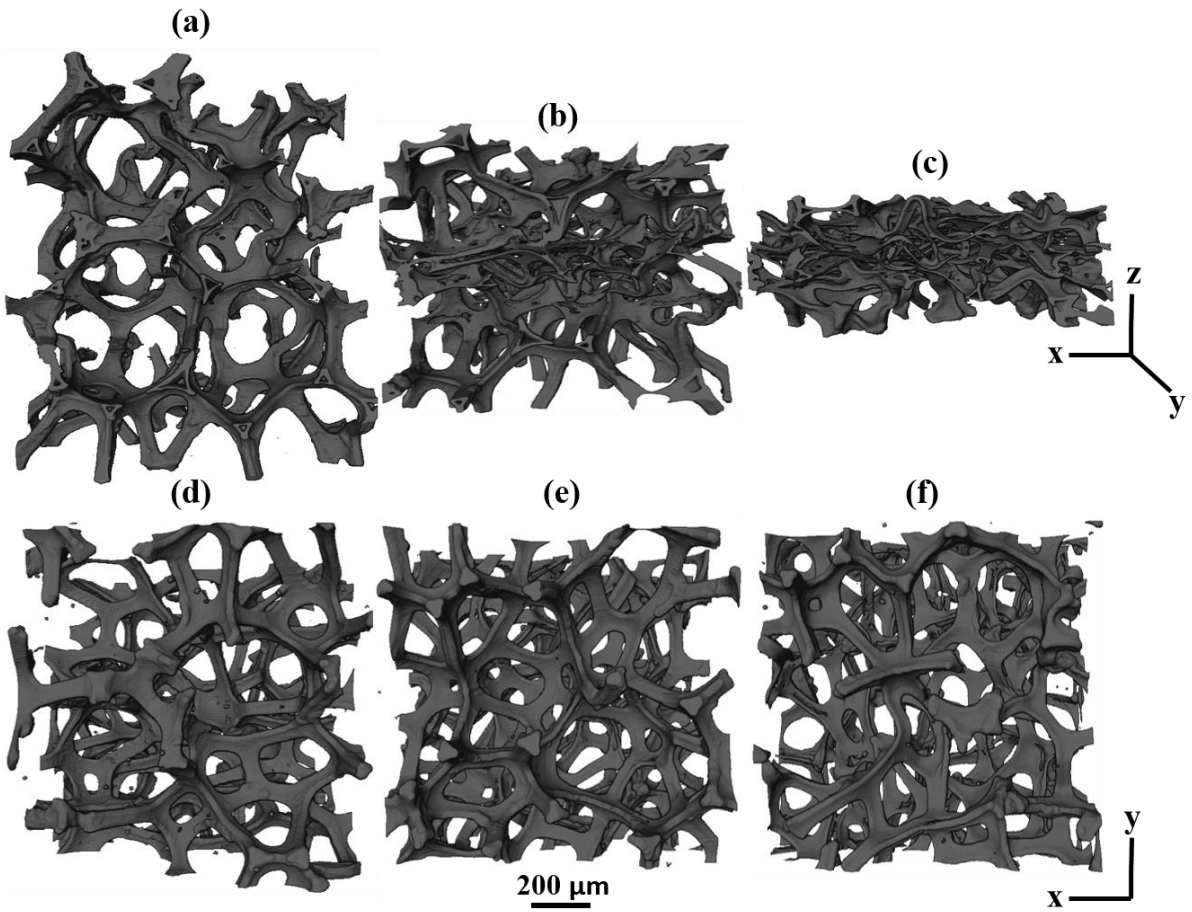

Fig. 3 Side view (a-c) and top view (d-f) of the reconstructed volume of the compressed metal foams; (a, d) 6 % compression, (b, e) 37 % compression, and (c, f) 69 % compression.

The Avizo software package was employed to extract the equivalent pore network of the metal foams. The pore phase was firstly segmented using grayscale thresholding method, followed by a watershed algorithm [67] to distinguish the boundary and separate individual pores. The pores were approximated to spherical shape with the size measured in terms of the equivalent radius. This simplified representation is used only for illustrative purposes, as in gas transport modelling, the network contains irregular pores that were directly extracted from the reconstructed images.

Fig. 4 (a-c) shows the 3D extracted pore network of compressed metal foam samples, where the void space was represented as ideal spherical pores of different sizes, and the pore size is measured as equivalent pore radius. The throats are also shown to indicate the inter-connection between neighbouring pores. A broad range of the pore size with heterogeneous spatial distribution is observed in the 6 % and 37 % compression sample, although the average pore size is much lower in 37 %

compression. 69% compression considerably reduces the average pore size and increases the homogeneity.

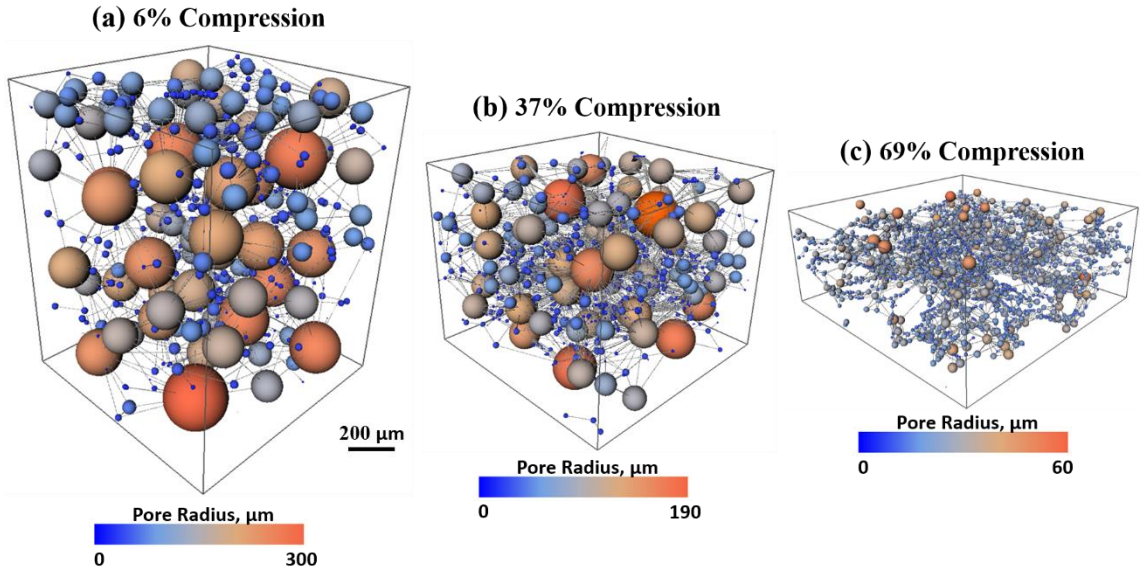

Fig. 4 (a-c) Illustration of the equivalent pore network in 3D where each pore was idealized as a sphere and was coloured according to its equivalent diameter. The grey lines between each pore show their connectivity.

The pore size distribution (PSD) and the corresponding cumulative frequencies for the metal foams under different compression levels are shown in Fig. 5 (a-c). The foam under minimum compression (6 %) shows a wide pore size distribution in the range of 0-300 µm, with two dominant peaks around 5-10 µm and 35-40 µm, and 10 % of pores are > 120 µm. The pore size distribution of the foam under medium compression (37 %) is relatively narrow (0-190 µm), where a dominant pore size peaks around 8-11 µm and pores with diameter ≤ 38 µm constitute about 90 % of pores. The foam under maximum compression (69 %) yields more narrowly distributed pore sizes, with 90 % of pores with diameter ≤25 µm. The result indicates that the compression process significantly decreases the mean pore size and narrows the PSD of metal foams.

Fig. 5 (d) presents the porosity and tortuosity factor of the metal foam samples under different compression levels. The porosity values are 95.5 %, 94.2 % and 90.8 % for the minimum (6 %), medium (37 %) and maximum (69 %) compressed metal foams, respectively. The foam under maximum compression leads to only a ~4 % and ~5 % decrease in porosity compared to the medium and

minimum compression. This indicates the foam retains a highly porous characteristic even under a high compression ratio. In terms of tortuosity, the values are 1.02, 1.03 and 1.09 for the minimum (6 %), medium (37 %) and maximum (69 %) compressed metal foams, respectively.

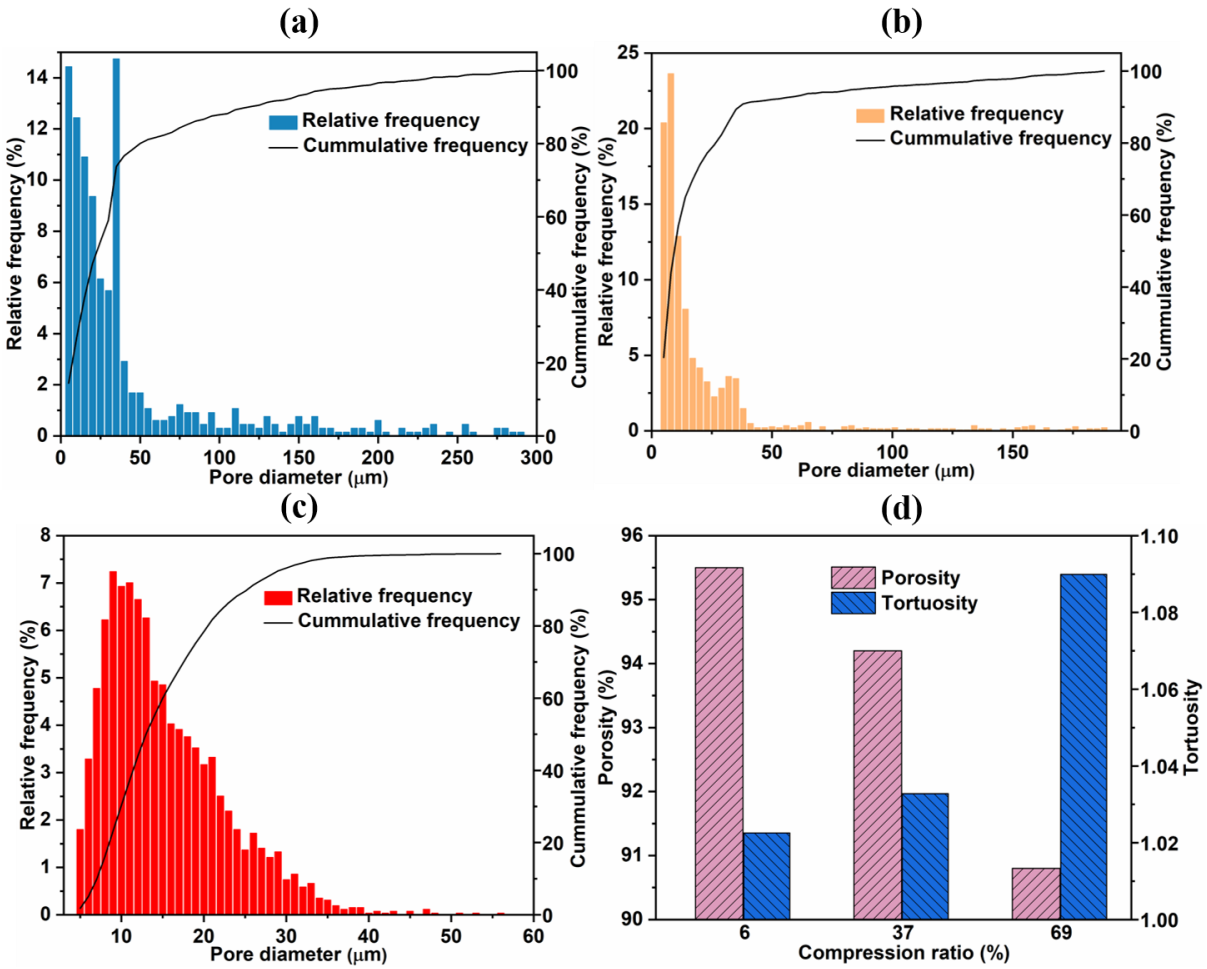

Fig. 5 (a-c) Pore size distribution, (d) porosity and tortuosity of metal foams under different compression levels: (a) 6 % compression, (b) 37 % compression, and (c) 69 % compression.

Understanding the gas transport within compressed metal foams and its relationship with PEFC performance is of critical importance for optimizing design rules of metal foam based flow-field. Numerical modelling provides an approach for studying the gas transport through the compressed metal foams. Thus, a numerical model for predicting gas transport would be extremely useful for determining the impact of metal foam structure on redistribution of air velocity and pressure. Fig. 6 shows the simulated distribution of air velocity in the metal foams under different compression levels (6 %, 1.5 mm; 37 %, 1 mm; 69 %, 0.5 mm). Given a constant mass flow rate of the air at the inlet (2.82 e^{-5} g s^{-1}),

the fluid velocity is observed to be inversely proportional to the compression level. Moreover, it is noted that the framework of the metal foam significantly slows down the air flow around it due to the viscous shear flow. This is more clearly seen in the zoomed in image of Fig. 6 (b), where the air streams clearly decelerate at the skeleton surface.

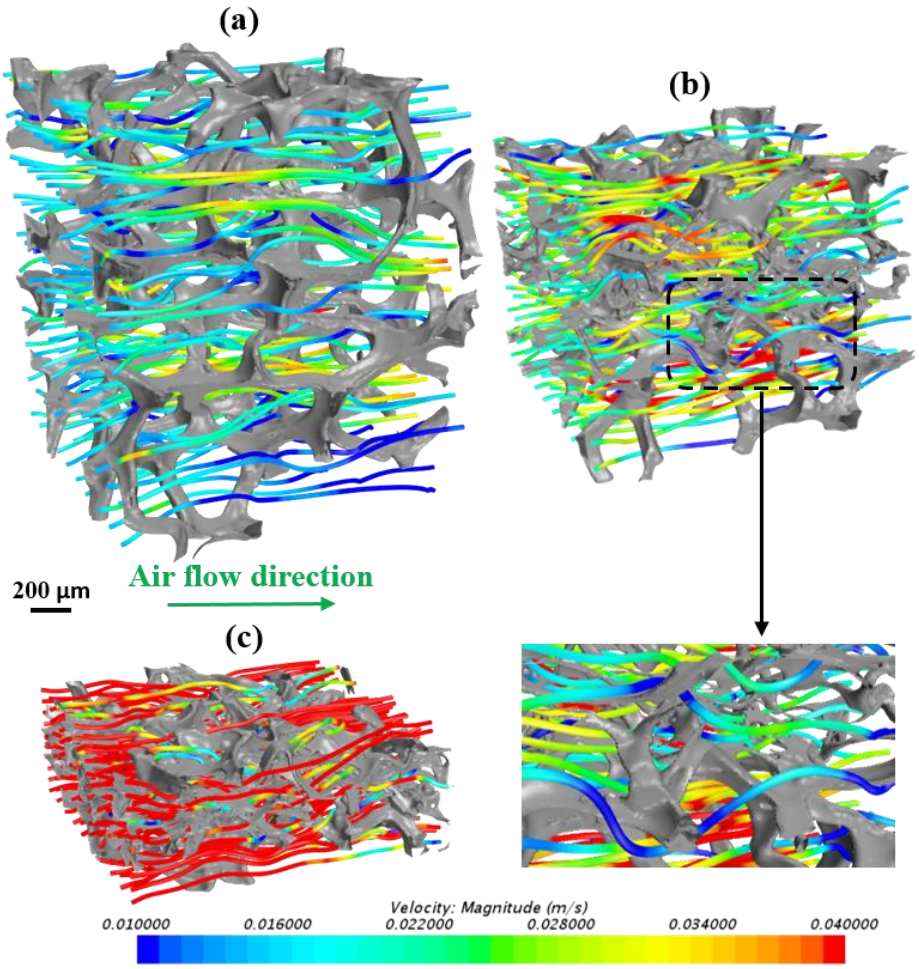

Fig. 6 Distribution of air velocity of metal foams under different compression levels: (a) 6 % compression, (b) 37 % compression, and (c) 69 % compression.

Fig. 7 (a-c) demonstrates that, as expected, under the same overall inlet air flow rate, a larger pressure gradient develops in highly compressed foams. The disparity of pressure gradient between low (6%) and medium (37%) compression is much lower compared to high (69%) compression sample, as a consequence of the remarkably increased mass transport resistance arising from lower in-plane porosity/pore size and higher viscous effect. Fig. 7 (d) presents the pressure drop and permeability of the metal foam samples under different compression levels. The pressure drop values are 0.09, 0.22 and

1.17 Pa for the minimum, medium and maximum compressed metal foams, respectively. The foam under maximum compression shows ~12 times and ~4 times larger pressure drop compared to the minimum and medium compression. Lower pressure drop in PEFCs with minimum and medium compression may increase the susceptibility to flooding. However, excess pressure drop from high compression is unfavourable from a viewpoint of power required to pressurize/recirculate the reactants. Therefore, a trade-off has to be struck between water management and parasitic power. In terms of permeability, the values are 4.22×10^{-9}, 2.45×10^{-9} and 0.996×10^{-9} m^2 for the minimum, medium and maximum compressed metal foams, respectively. This suggests that increasing the compression pressure renders higher resistance of the gas flow in the metal foam samples.

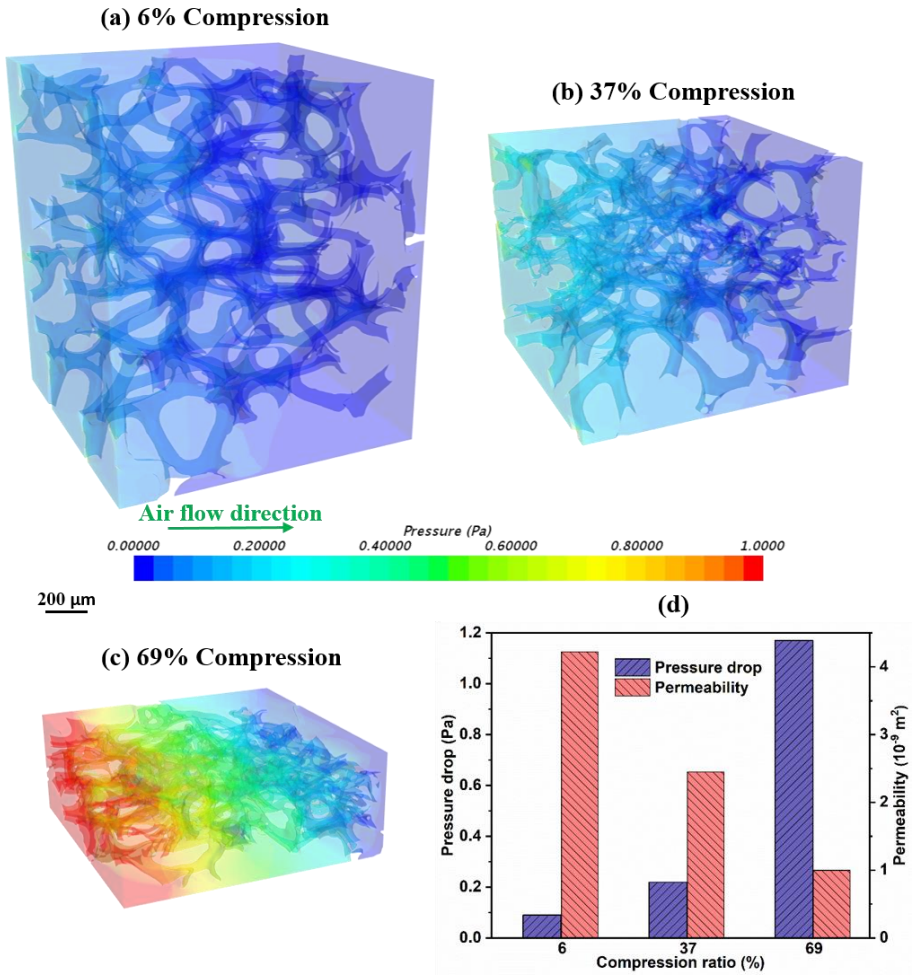

Fig. 7 (a-c) Distribution of pressure, (d) pressure drop and permeability of metal foams under different compression levels.

Fig. 8 (a-c) compares the averaged liquid water thickness distribution in the PEFCs with different compressed (6 %, 37 % and 69 %) metal foams during galvanostatic operation at 500 mA cm^{-2} (average current density) over 1200 s. In general, the increased compression ratio leads to a decrease in liquid water accumulation. Back-diffusion phenomenon of water from the cathode to the anode (vertical channels) is observed for all cases, with the highest anode water accumulation recorded at the minimum compression case, followed by medium and maximum compression. In terms of cathode water distribution, the liquid content within the maximum compression case (Fig. 8 (c)) appears across a much narrower region of the active area, compared to the minimum (Fig. 8 (a)) and medium compression (Fig. 8 (b)), indicating compressing the metal foam can alleviate flooding in PEFCs.

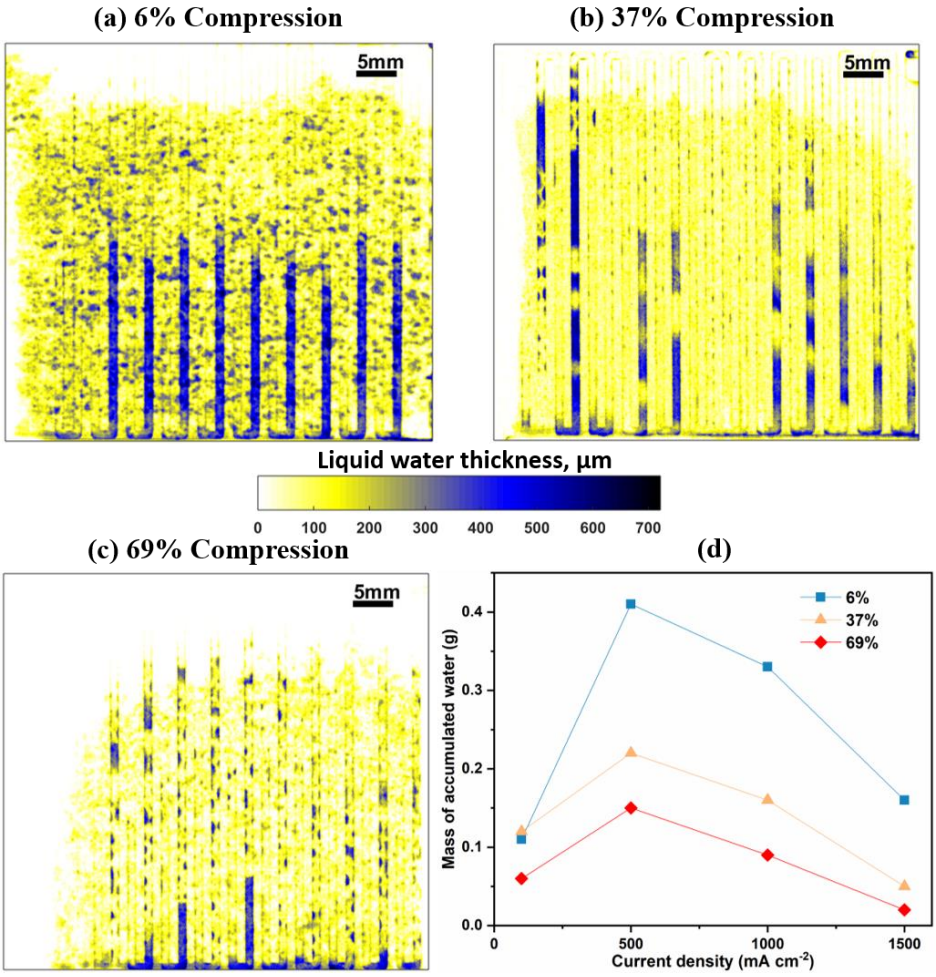

Fig. 8 (a-c) Effect of compression ratio (6%, 37% and 69%) on averaged liquid water thickness distribution during galvanostatic operation at 500 mA cm^{-2}. (d) Water accumulation of PEFCs under different levels of compression as a function of current density.

The water mass in the PEFC during galvanostatic operation was calculated based on the total water content across the active area of the averaged neutron image [15]. Fig. 8 (d) shows the change in water mass with respect to current density. Similar water accumulation trend is observed for different compression ratios; water continues to accumulate in the channel at low current density and starts to decline beyond 500 mA cm^{-2} as it evaporates. The results also indicate that much less liquid water is present in the PEFC with maximum compression (69 %) than the medium (37 %) and minimum compression (6 %) throughout the investigated operating range. At 500 mA cm^{-2}, the PEFC with minimum compression demonstrates a ~86 % and ~173 % increase in the mass of accumulated liquid water compared to the medium and maximum compression, respectively. A decreased susceptibility to flooding is found with increased compression ratio. This can be attributed to the higher pressure drop and gas velocity within the PEFC with larger compression, fostering effective convective liquid water removal as shown in Fig. 6 and Fig. 7. Once again, the results indicate that increasing the compression ratio of metal foam can facilitate the water removal ability of PEFCs, but at the cost of higher parasitic power. Overall, the PEFC with medium compression not only achieves the best performance, but can also be regarded as a judicious option from both water management and performance viewpoint.

Conclusion

Understanding how the extent of compression of metal foam flow-field affects the microstructural properties, gas transport parameters and water management characteristics in PEFCs is indispensable for optimizing the performance and durability. *In-operando* neutron radiography has been employed to visualize liquid water distribution across PEFCs with metal foams under three different compression ratios, and we present important steps made to characterize the microstructural properties of compressed metal foam samples using X-ray CT. The pore structures extracted from X-ray CT images are applied to simulate the gas transport in metal foams under different compression ratios. The conclusions are summarized as follows:

1) The PEFC performance is strongly affected by the compression ratio of metal foams. The peak power density of 853 mW $cm^{-2}$was recorded for PEFC with medium compression, followed by maximum (780

mW cm^{-2}) and minimum compression (568 mW cm^{-2}). The increasing compression ratio also leads to a decrease in Ohmic resistance.

2) X-ray CT data indicates that the compression process significantly decreases the mean pore size and narrows the PSD of metal foams. Though compression from 6% to 69% does not drastically reduce the overall porosity, the pore size and tortuosity in the flow direction are severely affected. The compactness of metal foam after heavy compression also yields a large viscous effect due to the increased volume specific area of the metal foam.

3) The simulation results demonstrate that the foam under maximum compression shows a ~12 times and ~4 times larger pressure drop compared to the minimum and medium compression, respectively. The larger pressure drop and resultant faster gas flow of PEFC with higher compression ratio improve the convective liquid removal.

4) Neutron images show that the PEFC with minimum compression demonstrates a ~86 % and ~173 % increase in the mass of accumulated liquid water (during galvanostatic operation at 500 mA cm^{-2}) compared to the medium and maximum compression, respectively. However, it would require higher parasitic power to pressurize/recirculate the reactants for the high compression case.

Overall, the PEFC with medium compression not only achieves the best performance compared to its counterparts, but can also be regarded as a reasonable trade-off condition.

Acknowledgements

The authors gratefully acknowledge the funding from the EPSRC (EP/S018204/2, EP/P009050/1 and EP/R023581/1) for supporting Electrochemical Innovation Lab and to the China Scholarship Council, UCL Faculty of Engineering Sciences Dean's Scholarship, STFC Futures Early Career Award (ST/R006873/1) and Sichuan Province Science and Technology Fund (2019YJ0236) for supporting Wu Yunsong.

References

[1] D.J.L. Brett, N.P. Brandon, Review of materials and characterization methods for polymer electrolyte fuel cell flow-field plates, J. Fuel Cell Sci. Technol 2007; 4(1): 29-44.

[2] S. Toghyani, E. Afshari, E. Baniasadi, Metal foams as flow distributors in comparison with serpentine and parallel flow fields in proton exchange membrane electrolyzer cells, Electrochimica Acta 2018; 290:506-519.
[3] W. Zuo, Q. Li, Z. He, Y. Li, Numerical investigations on thermal performance enhancement of hydrogen-fueled micro planar combustors with injectors for micro-thermophotovoltaic applications, Energy 2020; 194:116904.
[4] Q. Li, W. Zuo, Y. Zhang, J. Li, Z. He, Effects of rectangular rib on exergy efficiency of a hydrogen-fueled micro combustor, Int. J. Hydrogen Energy 2020; 45(16):10155-10163.
[5] W. Zuo, J. Li, Y. Zhang, Q. Li, S. Jia, Z. He, Multi-factor impact mechanism on combustion efficiency of a hydrogen-fueled micro-cylindrical combustor, Int. J. Hydrogen Energy 2020; 45(3): 2319-2330.
[6] V. Mehta, J.S. Cooper, Review and analysis of PEM fuel cell design and manufacturing, J. Power Sources 2003;114(1):32-53.
[7] S. Shimpalee, S. Greenway, J.W. Van Zee, The impact of channel path length on PEMFC flow-field design, J. Power Sources 2006; 160(1):398-406.
[8] J. Scholta, G. Escher, W. Zhang, W. Lehnert, Investigation on the influence of channel geometries on PEMFC performance, J. Power Sources 2006;155(1):66-71.
[9] X. Li, I. Sabir, Review of bipolar plates in PEM fuel cells: Flow-field designs, Int. J. Hydrogen Energy 2005; 30(4):359-71.
[10] J. Wang, Theory and practice of flow field designs for fuel cell scaling-up: A critical review, Appl Energy 2015; 157: 640-63.
[11] A. Ghanbarian, M.J. Kermani, J. Scholta, M. Abdollahzadeh, Polymer electrolyte membrane fuel cell flow field design criteria – Application to parallel serpentine flow patterns, Energy Convers. Manag 2018; 166: 281-96.
[12] A.P. Sasmito, J.C. Kurnia, A.S. Mujumdar, Numerical evaluation of various gas and coolant channel designs for high performance liquid-cooled proton exchange membrane fuel cell stacks, Energy 2012; 44(1):278-91.
[13] X. Wang, W. Yan, Y. Duan, F. Weng, G. Jung, C. Lee, Numerical study on channel size effect for proton exchange membrane fuel cell with serpentine flow field, Energy Convers. Manag 2010; 51(5):959-68.
[14] P. Trogadas, J.I.S. Cho, T.P. Neville, J. Marquis, B. Wu, D.J.L. Brett, M.O. Coppens, A lung-inspired approach to scalable and robust fuel cell design, Energy Environ. Sci 2018; 11(1):136-43.
[15] Y. Wu, J.I.S. Cho, T.P. Neville, Q. Meyer, R. Zeische, P. Boillat, M. Cochet, P.R. Shearing, D.J.L. Brett, Effect of serpentine flow-field design on the water management of polymer electrolyte fuel cells: An in-operando neutron radiography study, J. Power Sources. 2018; 399:254-63.
[16] N. Limjeerajarus, P. Charoen-Amornkitt, Effect of different flow field designs and number of channels on performance of a small PEFC, Int. J. Hydrogen Energy.2015;40(22):7144-58.
[17] A.D. Santamaria, N.J. Cooper, M.K. Becton, J.W. Park, Effect of channel length on interdigitated flow-field PEMFC performance: a computational and experimental study, Int. J. Hydrogen Energy. 2013;38(36):16253-63.
[18] N. Guo, M.C. Leu, U.O. Koylu, Bio-inspired flow field designs for polymer electrolyte membrane fuel cells, Int. J. Hydrogen Energy.2014;39(36):21185-95.
[19] C.E. Damian-Ascencio, A. Saldaña-Robles, A. Hernandez-Guerrero, S. Cano-Andrade, Numerical modeling of a proton exchange membrane fuel cell with tree- like flow field channels based on an entropy generation analysis, Energy.2017;133:306-16.
[20] N. Guo, M.C. Leu, U.O. Koylu, Network based optimization model for pin-type flow field of polymer electrolyte membrane fuel cell, Int. J. Hydrogen Energy.2013;38(16):6750-61.
[21] M. Whiteley, J.I.S. Cho, L. Rasha, T. Neville, J. Millichamp, R. Luca, P.R. Shearing, D.J.L. Brett, A novel polymer electrolyte fuel cell flow-field : The through-plane array, J. Power Sources. 2019;442:227218.
[22] J.I.S. Cho, T.P. Neville, P. Trogadas, J. Bailey, P. Shearing, D.J.L. Brett, M. Coppens, Capillaries for water management in polymer electrolyte membrane fuel cells, Int. J. Hydrogen Energy 2018; 43(48):21949-58.
[23] A. Kumar, R.G. Reddy, Modeling of polymer electrolyte membrane fuel cell with metal foam in the flow-field of the bipolar/end plates, J. Power Sources 2003; 114(1):54-62.

[24] Z. Bao, Z. Niu, K. Jiao, Numerical simulation for metal foam two-phase flow field of proton exchange membrane fuel cell, Int. J. Hydrogen Energy 2019; 44(12):6229-44.
[25] T. Kariya, T. Hirono, H. Funakubo, T. Shudo, Effects of the porous structures in the porous flow field type separators on fuel cell performances, Int. J. Hydrogen Energy 2014;39(27):15072-80.
[26] W. Yuan, Y. Tang, X. Yang, Z. Wan, Porous metal materials for polymer electrolyte membrane fuel cells–A review, Appl. Energy 2012; 94:309-29.
[27] D.K. Shin, J.H. Yoo, D.G. Kang, M.S. Kim, Effect of cell size in metal foam inserted to the air channel of polymer electrolyte membrane fuel cell for high performance, Renew. Energy 2018; 115:663-75.
[28] M. Kozakai, K. Date, Y. Tabe, T. Chikahisa, Improving gas diffusivity with bi-porous flow-field in polymer electrolyte membrane fuel cells, Int. J. Hydrogen Energy 2016; 41(30) 13180-9.
[29] S. Huo, N. James, T. Lee, J. Wan, K. Jiao, Experimental investigation on PEM fuel cell cold start behavior containing porous metal foam as cathode flow distributor, Appl. Energy 2017; 203:101-14.
[30] J.E. Park, W. Hwang, M.S. Lim, S. Kim, C.Y. Ahn, O.H. Kim, J.G. Shim, D.W. Lee, J.H. Lee, Y.H. Cho, Y.E. Sung, Achieving breakthrough performance caused by optimized metal foam flow field in fuel cells, Int. J. Hydrogen Energy 2019; 44(39):22074-84.
[31] A. Jo, H. Ju, Numerical study on applicability of metal foam as flow distributor in polymer electrolyte fuel cells (PEFCs), Int. J. Hydrogen Energy 2018; 43(30):14012-26.
[32] A. Jo, S. Ahn, K. Oh, W. Kim, H. Ju, Effects of metal foam properties on flow and water distribution in polymer electrolyte fuel cells (PEFCs), Int. J. Hydrogen Energy 2018; 43(30):14034-46.
[33] Y. Tabe, T. Nasu, S. Morioka, T. Chikahisa, Performance characteristics and internal phenomena of polymer electrolyte membrane fuel cell with porous flow field, J. Power Sources 2013; 238:21-8.
[34] A. Fly, D. Butcher, Q. Meyer, M. Whiteley, A. Spencer, C. Kim, P.R. Shearing, D.J.L. Brett, R. Chen, Characterisation of the diffusion properties of metal foam hybrid flow-fields for fuel cells using optical flow visualisation and X-ray computed tomography, J. Power Sources 2018; 395:171-8.
[35] J.E. Park, J. Lim, S. Kim, I. Choi, C.Y. Ahn, W. Hwang, M.S. Lim, Y.H. Cho, Y.E. Sung, Enhancement of mass transport in fuel cells using three-dimensional graphene foam as flow field, Electrochim. Acta 2018; 265:488-96.
[36] A. Fly, Q. Meyer, M. Whiteley, F. Iacoviello, T. Neville, P.R. Shearing, D.J.L. Brett, C. Kim, R. Chen, X-ray tomography and modelling study on the mechanical behaviour and performance of metal foam flow-fields for polymer electrolyte fuel cells, Int. J. Hydrogen Energy 2019; 44(14): 7583-95.
[37] J. Eun, J. Lim, M. Su, S. Kim, O. Kim, D. Woog, J. Hyun, Y. Cho, Y. Sung, Gas diffusion layer/flow-field unified membrane-electrode assembly in fuel cell using graphene foam, Electrochim. Acta.2019;323:134808.
[38] Y. Awin, N. Dukhan, Experimental performance assessment of metal-foam flow fields for proton exchange membrane fuel cells, Appl. Energy 2019; 252:113458-65.
[39] S. Cooper, D. Eastwood, J. Gelb, G. Damblanc, D. Brett, R. Bradley, P. Withers, P. Lee, A. Marquis, N. Brandon, Image based modelling of microstructural heterogeneity in LiFePO4 electrodes for Li-ion batteries, J. Power Sources. 2014; 247:1033-9.
[40] B. Tjaden, J. Lane, P.J. Withers, R.S. Bradley, D.J. Brett, P.R. Shearing, The application of 3D imaging techniques, simulation and diffusion experiments to explore transport properties in porous oxygen transport membrane support materials, Solid State Ionics.2016; 288:315-21.
[41] Y.-c.K. Chen-Wiegart, R. DeMike, C. Erdonmez, K. Thornton, S.A. Barnett, J. Wang, Tortuosity characterization of 3D microstructure at nano-scale for energy storage and conversion materials, J. Power Sources.2014;249:349-56.
[42] Y.-c. Karen Chen-Wiegart, J.S. Cronin, Q. Yuan, K.J. Yakal-Kremski, S.A. Barnett, J. Wang, 3D Non-destructive morphological analysis of a solid oxide fuel cell anode using full-field X-ray nano-tomography, J. Power Sources.2012;218:348-51.

[43] X. Lu, O.O. Taiwo, A. Bertei, T. Li, K. Li, D.J.L. Brett, P.R. Shearing, Multi-length scale tomography for the determination and optimization of the effective microstructural properties in novel hierarchical solid oxide fuel cell anodes, J. Power Sources. 2017;367:177-86.
[44] X. Lu, B. Tjaden, A. Bertei, T. Li, K. Li, D. Brett, P. Shearing, 3D Characterization of Diffusivities and Its Impact on Mass Flux and Concentration Overpotential in SOFC Anode, J. Electrochem. Soc,2017;164:188-95.
[45] X. Lu, T. Li, A. Bertei, J.I.S. Cho, T.M.M. Heenan, M.F. Rabuni, K. Li, D.J.L. Brett, P. R. Shearing, The application of hierarchical structures in energy devices: new insights into the design of solid oxide fuel cells with enhanced mass transport, Energy Environ. Sci. 11 (2018) 2390-403.
[46] X. Lu, A. Bertei, T.M.M. Heenan, Y. Wu, D.J. Brett, P.R. Shearing, Multi-length scale microstructural design of micro-tubular Solid Oxide Fuel Cells for optimised power density and mechanical robustness, J. Power Sources, 2019:434:226744.
[47] X. Lu, A. Bertei, D.P. Finegan, C. Tan, S.R. Daemi, J.S. Weaving, K.B.O. Regan, T.M.M. Heenan, G. Hinds, E. Kendrick, D.J.L. Brett, P.R. Shearing, 3D microstructure design of lithium-ion battery electrodes assisted by X-ray nano-computed tomography and modelling, Nature Communications 11.1 (2020): 1-13.
[48] I. V. Zenyuk, D.Y. Parkinson, L.G. Connolly, A.Z. Weber, Gas-diffusion-layer structural properties under compression via X-ray tomography, J. Power Sources,2016;328:364-76.
[49] N. Kulkarni, J.I.S. Cho, L. Rasha, R.E. Owen, Y. Wu, R. Ziesche, J. Hack, T. Neville, M. Whiteley, N. Kardjilov, I. Manke, P.R. Shearing, D.J.L. Brett, H. Mark, Effect of cell compression on the water dynamics of a polymer electrolyte fuel cell using in-plane and through-plane in-operando neutron radiography, J. Power Sources, 2019;439: 227074.
[50] J. Hack, T.M.M. Heenan, F. Iacoviello, N. Mansor, Q. Meyer, P. Shearing, N. Brandon, D.J.L. Brett, A structure and durability comparison of membrane electrode assembly fabrication methods: self-assembled versus hot-pressed, J. Electrochem. Soc,2018;165:3045-52.
[51] I. Tolj, D. Bezmalinovic, F. Barbir, Maintaining desired level of relative humidity throughout a fuel cell with spatially variable heat removal rates, Int. J. Hydrogen Energy 2011; 36(20):13105-13.
[52] C. Lebreton, M. Benne, C. Damour, N. Yousfi-Steiner, B. Grondin-Perez, D. Hissel, J.P. Chabriat, Fault Tolerant Control Strategy applied to PEMFC water management, Int. J. Hydrogen Energy 2015; 40(33):10636-46.
[53] L. Zhang, M. Pan, S. Quan, Model predictive control of water management in PEMFC, J. Power Sources, 2008;180:322-9.
[54] R. Mosdale, G. Gebel, M. Pineri, Water profile determination in a running proton exchange membrane fuel cell using small-angle neutron scattering, J. Membr. Sci,1996;118 (2):269-77.
[55] R. Satija, D.L. Jacobson, M. Arif, S.A. Werner, In situ neutron imaging technique for evaluation of water management systems in operating PEM fuel cells, J. Power Sources,2004;129(2):238-45.
[56] J.P. Owejan, T.A. Trabold, D.L. Jacobson, M. Arif, S.G. Kandlikar, Effects of flow field and diffusion layer properties on water accumulation in a PEM fuel cell, Int. J. Hydrogen Energy 2007; 32(17):4489-502.
[57] Y. Wu, J.I.S. Cho, X. Lu, L. Rasha, T.P. Neville, J. Millichamp, R. Ziesche, N. Kardjilov, H. Markötter, P. Shearing, D.J.L. Brett, Effect of compression on the water management of polymer electrolyte fuel cells : An in-operando neutron radiography study, J. Power Sources 2019; 412:597-605.
[58] J.I.S. Cho, T.P. Neville, P. Trogadas, Q. Meyer, Y. Wu, R. Ziesche, P. Boillat, M. Cochet, V. Manzi-orezzoli, P. Shearing, D.J.L. Brett, Visualization of liquid water in a lung-inspired flow-field based polymer electrolyte membrane fuel cell via neutron radiography, Energy 2019; 170: 14-21.
[59] E. Coz, J. Théry, P. Boillat, V. Faucheux, D. Alincant, P. Capron, G. Gébel, Water management in a planar air-breathing fuel cell array using operando neutron imaging, J. Power Sources 2016; 331:535-43.
[60] Y. Wu, Q. Meyer, F. Liu, L. Rasha, J.I.S. Cho, T.P. Neville, J. Millichamp, R. Ziesche, N. Kardjilov, P. Boillat, H. Markötter, I. Manke, M. Cochet, P. Shearing, D.J.L. Brett, Investigation of water generation and accumulation in polymer electrolyte fuel cells using hydro-electrochemical impedance imaging, J. Power Sources 2019; 414:272-7.

[61] Q. Meyer, S. Ashton, R. Jervis, D.P. Finegan, P. Boillat, M. Cochet, O. Curnick, T. Reisch, P. Adcock, P.R. Shearing, D.J.L. Brett, The Hydro-electro-thermal Performance of Air-cooled, Open-cathode Polymer Electrolyte Fuel Cells: Combined Localised Current Density, Temperature and Water Mapping, Electrochim. Acta 2015;180:307-15.

[62] Y. Wu, J.I.S. Cho, M. Whiteley, L. Rasha, T.P. Neville, R. Ziesche, R. Xu, R. Owen, N. Kulkarni, J. Hack, M. Maier, I. Manke, F.R. Wang, P.R. Shearing, D.J.L. Brett, Characterization of water management in metal foam flow-field based polymer electrolyte fuel cells using in-operando neutron radiography, Int. J. Hydrogen Energy 2020;45:2195-05.

[63] H. Darcy, Les fontaines publiques de la ville de Dijon: exposition et application, Victor Dalmont, 1856.

[64] Kardjilov, N., Hilger, A. and Manke, I. "Conrad-2: cold neutron tomography and radiography at ber ii (v7)." Journal of large-scale research facilities JLSRF 2016; 2: 98.

[65] D.J.L. Brett, S. Atkins, N.P. Brandon, N. Vasileiadis, V. Vesovic, A.R. Kucernak, Membrane resistance and current distribution measurements under various operating conditions in a polymer electrolyte fuel cell, J. Power Sources 2007; 172(1):2-13.

[66] V.A.R. Ilie, S. Martemianov, A. Thomas, Investigation of the local temperature and overheat inside the membrane electrode assembly of PEM fuel cell, Int. J. Hydrogen Energy 2016; 41(34): 15528-37.

[67] https://assets.thermofisher.com/TFS-Assets/MSD/Product-Guides/user-guide-avizo-software.pdf.